Ab initio study of the dynamics of electron trapping and detrapping processes in the CH₃NH₃PbI₃ perovskite

Journal:	*Journal of Materials Chemistry A*
Manuscript ID	TA-ART-10-2018-009512.R1
Article Type:	Paper
Date Submitted by the Author:	07-Dec-2018
Complete List of Authors:	Zhang, Linghai; City University of Hong Kong, Sit, Patrick; City University of Hong Kong, School of Energy and Environment

Ab initio study of the dynamics of electron trapping and detrapping processes in the CH₃NH₃PbI₃ perovskite

Linghai Zhang [a], and Patrick H.-L. Sit [a,1]

[a] School of Energy and Environment, City University of Hong Kong, Kowloon,

Hong Kong S.A.R, China

Abstract

Charge trapping and detrapping are responsible for a number of unusual properties in the CH₃NH₃PbI₃ (MAPbI₃) perovskite such as photoinduced ion migration, photodegradation, and current density−voltage hysteresis. However, little is known about the dynamic processes of charge trapping and detrapping at the trap sites. Herein, the behavior of excess electron trapping and its interplay with iodine vacancies in the MAI–terminated and PbI₂–terminated MAPbI₃ surfaces were studied by density functional theory (DFT) calculations. The results show that the positively-charged iodine vacancy (V_I^+) is energetically more favorable to stay at the top-surface layer. By trapping excess electrons, the iodine vacancy migrates from the top-surface layer to the subsurface layer due to the formation of deep-level trap states. On the other hand, the adsorption of OH radicals and O₂ molecules induces electron detrapping from the deep-level trap states and iodine vacancies migration from the subsurface back to the top-surface layer. Furthermore, we studied the electron trapping and detrapping processes in bulk MAPbI₃. We found that in bulk MAPbI₃, the excess electrons facilitate the clustering of the iodine vacancies together and form deep trap states via the iodine migration process. However, electron detrapping was found to induce the hopping of two adjacent iodine vacancies away from each other. Our results show that while excess electrons trapped in both the shallow-level and deep-level states enhance photodegradation of MAPbI₃ under the humid air condition, the electrons in the deep-level traps play a significantly more important role in facilitating photoinduced ion migration and the hysteresis behavior.

---

[1]Corresponding Author, E-mail: patrick.h.sit@cityu.edu.hk. Phone: (852)34426709.

1. Introduction

A new generation of photovoltaic device utilizing hybrid metal–halide perovskites as the light–harvesting layers has recently emerged, showing superb power conversion efficiencies (PCEs) now surpassing 22%.[1-3] The hybrid metal-halide perovskites are crystalline materials with a chemical formula of ABX_3, where A is typically a monovalent organic cation such as $CH_3NH_3^+$ (MA) or $CH(NH_2)_2^+$ (FA); B is a divalent metal such as Pb^{2+} or Sn^{2+}; and X is a monovalent halide anion like I^-, Br^- or Cl^-.[4-7] This class of materials has attracted great interest in the past few years because of their outstanding performance such as long charge carrier diffusion lengths, tunable optical absorption, and low band gaps.[8-11]

Despite the high PCEs of the perovskite solar cells, the trapping of the free charge carriers by intrinsic defects and impurities is expected to limit the performance of this class of photovoltaic system.[12-15] Such trapped states play a significant role in the charge transport of perovskite solar cells. The shallow trapped states, which are close to the conduction or valence band edges, result in the decrease of charge carrier mobility. The deep trapped states, which are generally close to the middle of band gap, can serve as the nonradiative recombination centers, reducing the carrier lifetime and open circuit voltage.[16] Previous studies measured that the number densities of the shallow and deep trapped states in $CH_3NH_3PbI_3$ (MAPbI$_3$) films are around 10^{14}–10^{17} cm^{-3}.[17, 18] The presence of these trapped states is closely connected to photoinduced halide migration and are detrimental to the photo–stability of the perovskite materials.[19-22] For example, Stranks and coworkers observed photoinduced halide migration in the MAPbI$_3$ films in the presence of charge trapped states.[20] Aristidou et. al. showed that iodine vacancies in the MAPbI$_3$ films can be eliminated by the iodide anion from the salt, suppressing the formation of superoxide species from oxygen (O_2) and thus improving the stability of the perovskite materials.[21] Meanwhile, the photoluminescence (PL) intensity was also observed to increase when the perovskite is in contact with the atmosphere because the photoinduced intragap states were found to be passivated by O_2.[23-25] Besides, it has been suggested that charge trapping and detrapping at the trap sites is one of the origins of the current density–voltage (J–V) hysteresis[26-33] behavior when a large number

of charge carriers can be trapped under the forward bias condition and released under the short-circuit condition.[31, 32] Lee and coworkers showed that J–V hysteresis can be reduced by minimizing the trap density due to the reduction of nonradiative recombination.[29] Wang et. al. also found that J–V hysteresis was eliminated by using the fullerene derivative layers, which resolves the electron accumulation problem, resulting in the decrease of the trap density at the perovskite/fullerene derivative interfaces.[30]

Recently, the shallow and deep trapped states in the bulk, crystal surfaces and grain boundaries of metal-halide perovskites have been widely studied by density function theory (DFT) and time-dependent DFT (TDDFT) calculations.[34-47] For example, previous DFT studies found the formation of the Pb–Pb covalent bond in the deep–level trap states such as antisite defect Pb_I and iodine vacancy V_I^-.[35-39, 45] The above calculations provide important insight on the properties of the trapped states of the perovskite materials. However, little is known about the dynamical processes of charge trapping and detrapping at the trap sites. As stated above, it has been found that photoinduced halide migration occurs in $MAPbI_3$ films in the presence of charge trapped states.[20] This means that defects such as iodine vacancies are mobile during charge trapping and detrapping. In other words, the iodine vacancies of different charges (i.e. V_I^+, V_I^0, V_I^-) are no longer confined to a specific lattice site when there are excess electrons or holes in the $MAPbI_3$ perovskite. To distinguish the different types of iodine vacancies, the superscripts +1, 0, and -1 denote the total charge of the systems after the vacancy is introduced.

The focus of this work is to study the iodine vacancies at the top-surface layer and subsurface layer of $MAPbI_3$ surfaces during the electron trapping and detrapping processes. The reason we place focus on the surface is that previous experimental studies showed that the trapped states (e.g., iodine vacancies) are generally located close to the crystal surfaces due to the presence of dangling bonds.[48, 49] Meanwhile, to consider the long-range ion migrations, we also studied the electron trapping and detrapping processes in bulk $MAPbI_3$. The paper is arranged as follows. In Section 2, we present the computational methodology adopted in this work. In Section 3, we discuss the study of the dynamics of charge trapping and detrapping process in the MAI–

terminated, PbI_2–terminated $MAPbI_3$ surfaces and bulk $MAPbI_3$. We first investigated the surface stability of V_I^+ vacancies in the two surfaces. Then, we studied the electron trapping process around the iodine vacancies. The electron detrapping process was also studied in the presence of the H_2O, OH radical and O_2 in the two surfaces. Finally, the electron trapping and detrapping process in bulk $MAPbI_3$ were also studied. We conclude our work in Section 4.

2. Computational methodology

At the room temperature, $MAPbI_3$ adopts a tetragonal structure with the bulk lattice parameters: a = 8.88 Å and c = 12.63 Å.[50] The MAI–terminated and PbI_2–terminated $MAPbI_3$ (110) surface were created by cleaving the bulk $MAPbI_3$. We chose the $MAPbI_3$ (110) surface as the prototypical model because it is of importance in the performance of perovskite solar cells.[51, 52] We built a ($\sqrt{2} \times \sqrt{2}$) surface supercell with 2.5 repeated slab of $MAPbI_3$. The corresponding chemical formulae are $(MAPbI_3)_{16}(MAI)_8$ and $(MAPbI_3)_{16}(PbI_2)_8$. From the compositions of the surface, we can regard them as MAI–excess and PbI_2–excess surfaces, respectively. The slabs were modeled by applying a vacuum gap of ~12 Å to separate the periodically repeated supercells. The surface model is the same as that of our previous work which has been tested to be adequate for the study.[53, 54] We further tested this surface model with an iodine vacancy and found that the 2.5-layer model is adequate for this study. Figure 1 shows the top-view and the side-view of the MAI-terminated and PbI_2-terminated (110) $MAPbI_3$ surfaces.

All the density functional theory (DFT)[55, 56] simulations were performed with the QUANTUM ESPRESSO package.[57] The simulations were carried out with the gamma point sampling of the Brillouin zone, which has been tested to be adequate. We performed spin-polarized calculations for the systems which have unpaired electrons (e.g. the structures with V_I^0, the adsorption of OH and O_2, etc.), while spin-unpolarized calculations were applied to the other systems. For the Perdew–Burke–Ernzerhof (PBE) exchange–correlation functional[58] calculations, we used the ultrasoft, scalar relativistic pseudopotentials[59] with the plane-wave kinetic energy cutoffs for the wavefunctions and the augmented charge density were 30 and 240 Ry, respectively. To better describe the weak interactions, the van der Waals (vdW) correction by Grimme and co-authors

was employed.[60, 61] Unless stated otherwise, the calculations reported in this work were performed at the PBE level with the above settings.

The adsorption energy of the adsorbates (i.e. H_2O, O_2 and OH) on the $MAPbI_3$ surfaces is defined as: $E_{ads} = E(adsorbate/MAPbI_3) - E(adsorbate) - E(MAPbI_3)$, where $E(adsorbate/MAPbI_3)$ is the total energy of the adsorbate on the $MAPbI_3$ slab, $E(adsorbate)$ is the energy of the adsorbate, and $E(MAPbI_3)$ is the energy of the $MAPbI_3$ slab. The activation energy for iodine migration on the perovskite surface was computed by using the climbing image nudged elastic band (CI–NEB) method.[62] The charge states of the different species on the perovskite surfaces (e.g. Pb ions) were determined by the maximally localized Wannier function (MLWF)[63, 64] analysis method, which has been applied in previous studies.[53, 54, 65, 66] The Wannier90 package[67] was employed to obtain the Wannier Centers (WCs) of the species, and the results of the charge states calculations are presented in the Supplementary Information (SI). Besides the calculations on the $MAPbI_3$ (110) surfaces, we also studied the electron trapping and detrapping behavior in bulk $MAPbI_3$. For the bulk calculations, we used the $2 \times 2 \times 1$ tetragonal $MAPbI_3$ supercell. The simulations were carried out with the $1 \times 1 \times 2$ grids of k-point sampling of the Brillouin zone.

For the defect-level calculations, we also performed single-point calculations using the Heyd−Scuseria−Ernzerhof (HSE) hybrid functional[68] (43% Hartree−Fock exchange) with the inclusion of the spin-orbit coupling (SOC) interactions, which was suggested by previous studies.[40, 45, 69, 70] The HSE+SOC calculations were performed using norm-conserving pseudopotentials on the optimized structures from the PBE functional calculations above. The plane-wave kinetic energy cutoffs for the wavefunctions here is 50 Ry. The k-point sampling mesh of each HSE+SOC calculation is the same as the corresponding calculation at the GGA-PBE level. The HSE+SOC method give a band gap of 1.45 eV for bulk $MAPbI_3$, which is in good agreement with the experimental band gap of 1.51 eV.[71] The energy levels of the defect states in the surface slabs were obtained from the Kohn−Sham levels as in the work by Yamashita and coworkers.[45] For the thermodynamic ionization levels $\varepsilon(q_1/q_2)$ of the iodine vacancy in bulk $MAPbI_3$, we used the equation: $\varepsilon(q_1/q_2) = [E_D(q_1) - E_D(q_2)]/(q_2 - q_1) - E_{VBM}$, where $E_D(q_1)$ and $E_D(q_2)$ are the total

DFT energies of the defective supercells with the charged states of q_1 and q_2 respectively, and E_{VBM} is the valence band maximum (VBM) of the pristine bulk MAPbI$_3$.
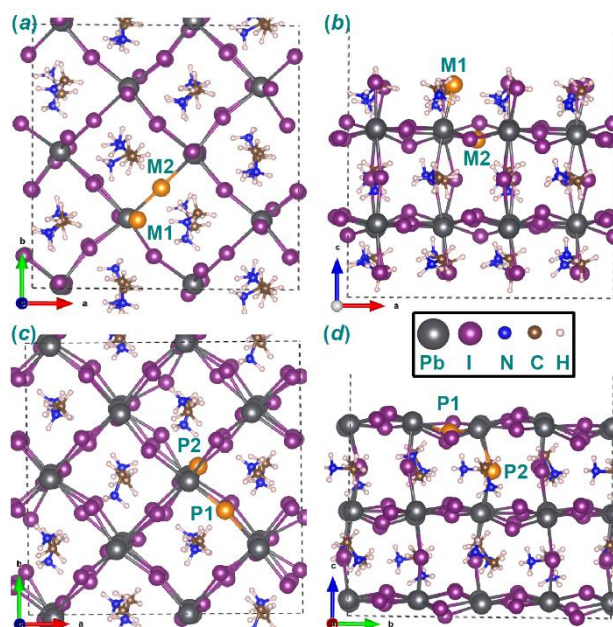

Figure 1. (a) & (b) Top view and side view of the relaxed MAI−terminated MAPbI$_3$ (110) surface, respectively. **M1** and **M2** (orange spheres) in the MAI−terminated surface are the selected iodine to create the iodine vacancies. (c) & (d) Top view and side view of the relaxed PbI$_2$−terminated MAPbI$_3$ (110) surface, respectively. **P1** and **P2** (orange spheres) in the PbI$_2$−terminated surface are the selected iodine to create the iodine vacancies.

3. Result and discussion

3.1 Electron trapping at the MAI–terminated surface

We first studied the positive iodine vacancies at the top-surface layer (at the **M1** position in Figure 1) and subsurface layer (at the **M2** position in Figure 1) of the MAI–terminated surface (MAI–excess condition). Without excess electrons, the charge state of iodine vacancy is +1 (V_I^+) after removal of an iodide ion. The optimized structures are respectively shown in Figures 2a and 2b. We obtained two similar structures as the iodide at the top-surface layer spontaneously migrated to the subsurface layer for the case when a vacancy was created at the subsurface **M2** position (Figure 2b), filling up the vacancy there. This means that the V_I^+ vacancy (**M2**) at the subsurface

layer is energetically unfavorable. The reason could be that creating the subsurface layer vacancy involves breaking two Pb–I bonds while only one Pb-I bond is broken when the top-surface layer vacancy is created.

We then studied the V_I^+ vacancy with an excess electron (i.e., V_I^0). The relaxed structures after introducing the excess electron to the structures with the top-surface layer vacancy and with the subsurface layer vacancy are shown in Figures 2c and 2d respectively. Since the systems have an unpaired electron, the figures also show the spin densities. For the case with the V_I^0 vacancy at the top-surface layer (Figure 2c), the excess electron delocalizes around the lead ions. The charge density difference (Figure SI1a in the SI) also confirms that the added electron in the structure in Figure 2c is delocalized. For case with the V_I^0 vacancy at the subsurface layer (Figure 2d), the added electron is partially trapped by the two Pb ions around the iodine vacancy, and spontaneous iodine diffusion was not observed. The charge density difference (Figure SI1b in the SI) also shows that the added electron in the structure in Figure 2d is partially trapped by the two Pb ions around the iodine vacancy. However, the V_I^0 vacancy at the top-surface layer is more stable by –6.1 kcal/mol compared to that at the subsurface layer. This is consistent with the simulation work of Meng and coworkers.[41] Similar to the case with the V_I^+ vacancy, the V_I^0 vacancy still prefers to stay at the top-surface layer, and there is no iodide migration induced by trapping one excess electron. As shown in Figure 2g, the total density of states (DOS) for the top-layer vacancy structure (Figure 2c) shows that there is no deep intragap states. We also plotted the DOS for the subsurface-layer vacancy structure (Figure 2d) and found that there is no deep intragap states (Figure SI2 in the SI). As will be discussed later, the presence of deep-level trapped states is closely related to the stability of the iodine vacancy at the subsurface layer.

We then studied the V_I^+ vacancy with two excess electrons (i.e., V_I^-). The optimized structures after introducing two excess electrons to the structures with the top-surface layer vacancy and with the subsurface layer vacancy are shown in Figures 2e and 2f respectively. The charge density difference (Figures SI1c and SI1d in the SI) shows that the added electron in the structure in Figure 2e is delocalized, while the added electron in the structure in Figure 2f is mainly localized at two

Pb ions. In contrast to the results above, the optimized structure in Figure 2f with the vacancy at the subsurface layer was found to be more stable by –10.4 kcal/mol than that in Figure 2e where the vacancy stays at the top-surface layer. It is due to the formation of a Pb–Pb covalent bond (ion distance: $d_{(Pb-Pb)}$ = 3.62 Å) at the subsurface layer. Previous DFT studies also observed Pb–Pb covalent bond formation in presence of the V_I^- defect for bulk MAPbI$_3$.[35, 38] The MLWF analysis showed that the two bonding Pb ions were reduced to form a Pb$_2^{2+}$ dimer (as shown in Figures SI3a and SI3b in the SI). This means that the two introduced electrons are strongly localized at the two Pb ions. This Pb dimer could be the precursor of formation of lead nanoparticles (one of the MAPbI$_3$ degradation products in vacuum).[72, 73] Moreover, as shown in Figure 2h, the total DOS for the structure in Figure 2f has a deep intragap state. Using the HSE functional with SOC, we also found the defect levels is located between the conduction band minimum (CBM) and valance band maximum (VBM) (shown in Figure SI4a in the SI), and a deep-level trap state is formed. This is in agreement with the results from the GGA-PBE method. Unlike V_I^+ and V_I^0, the V_I^- vacancy at the subsurface layer is energetically more favorable, suggesting that the two electrons in the deep-level trap enhances the stability of the iodine vacancy at the subsurface layer. Therefore, the iodine vacancy could migrate from the top-surface layer to the subsurface layer upon two-electron trapping. We performed the CI–NEB calculation to obtain the energy barrier for this process. As shown in Figure 2i, the activation energy is +7.0 kcal/mol. This is consistent with previous experimental measurement (+7.6 ~ + 13.8 kcal/mol)[74, 75] and DFT calculations (+1.4 ~ +15.0 kcal/mol).[74-78]
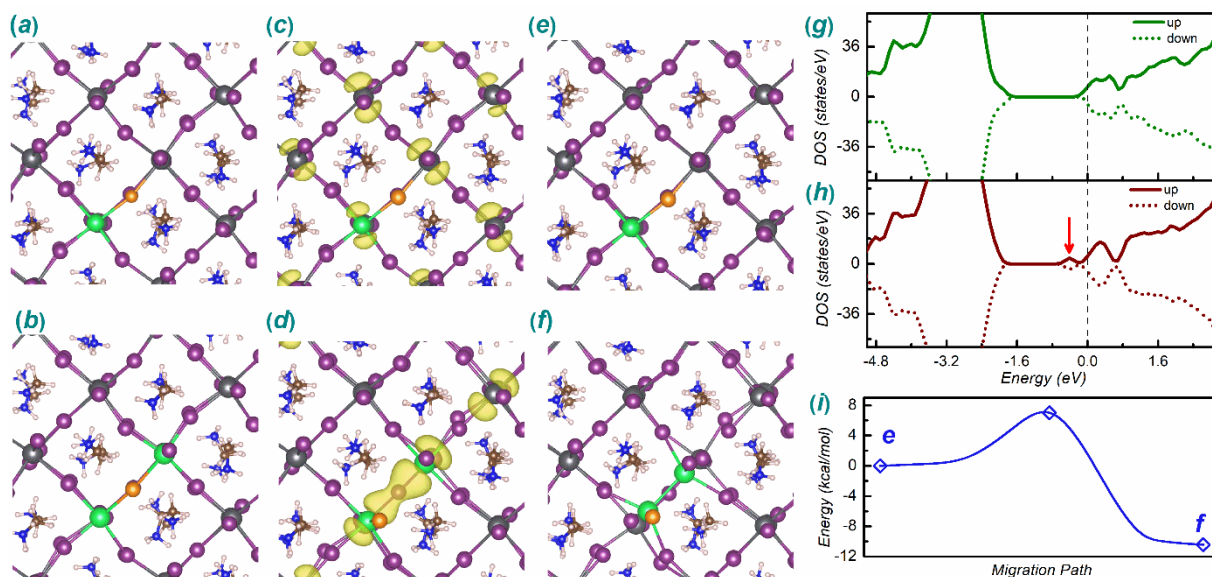
Figure 2. (a) & (b) The relaxed structure with a V_I^+ vacancy initially at the **M1** and the **M2** position, respectively, in the MAI−terminated surface. (c) & (d) The relaxed structure with a V_I^0 vacancy initially at the **M1** and the **M2** position, respectively, in the MAI−terminated surface. (e) & (f) The relaxed structure with a V_I^- vacancy initially at the **M1** and the **M2** position, respectively, in the MAI−terminated surface. (g) & (h) The total density of states for the structure in Figures 2c and 2f, respectively, with the Fermi level set at 0 eV. The red arrow in Figure 2h indicates the intragap trapped state. (i) The energy profile for the iodine migration from the structure in Figure 2e to the structure in Figure 2f. The side views of the structures in this figure are shown in Figure SI5 in the SI. The Pb ions originally bonded to the removed iodide are marked as green spheres. The spin densities are shown as the yellow contour surfaces. The color codes for the other atoms are the same as those in Figure 1.

3.2 Electron trapping at the PbI₂−terminated surface

We next studied the V_I^+ vacancy at the top-surface layer (marked as **P1** in Figure 1) and subsurface layer (marked as **P2** in Figure 1) of the PbI₂−terminated surface (PbI₂−excess condition). The optimized structures are shown in Figures 3a and 3b. Similar to the MAI-terminated surface, V_I^+ vacancy (**P2** position) at the subsurface layer is energetically unstable, and the surface iodide at the **P1** position spontaneously migrates to the **P2** position to fill up the vacancy. Although removing an iodide (I⁻) from the top-surface layer and from the subsurface layer both need to break two Pb–I bonds, the subsurface iodide (**P2** position) interacts with four MA cations while

there are only two MA cations that interact with the top-surface iodide at the **P1** position (as shown in Figures 1c and 1d). Therefore, creating a top-surface V_I^+ vacancy requires less energy.

We then studied the V_I^+ vacancy with an excess electron (i.e., V_I^0). The optimized structures after introducing one excess electron to the structures with the top-surface layer vacancy and the subsurface layer vacancy are shown in Figures 3c and 3d respectively. The figures also show the spin densities for the two cases. As shown in the figures, the excess electron delocalizes over different Pb ions for the case with the V_I^0 vacancy in the top layer, which agrees well with the previous DFT work.[45] The charge density difference (Figure SI6a in the SI) also confirms that the added electron in the structure in Figure 3c is delocalized. However, for the V_I^0 vacancy at the subsurface layer, the excess electron strongly localizes at the two Pb ions originally bonded to the removed iodide, forming a covalent Pb–Pb bond ($d_{(Pb\text{-}Pb)} = 3.57$ Å). The charge density difference (Figure SI6b in the SI) also shows that the added electron in the structure in Figure 3d is localized. The MLWF analysis showed that the two bonding Pb ions were reduced to form a Pb_2^{3+} dimer (Figures SI3c and SI3d in the SI). Unlike V_I^+, the V_I^0 at the subsurface layer is more stable by – 7.2 kcal/mol than that at the top-surface layer. Therefore, the iodine vacancy is likely to migrate from the top-surface layer to the subsurface layer during the one electron trapping process. We performed CI–NEB to study this migration (Figure 3i), and the activation energy was found to be +7.2 kcal/mol. For V_I^0 at the subsurface layer, the total DOS shown in Figure 3g and the spin density shown in Figure 3d show that there is a deep-level intragap trapped state with a localized electron. Using the HSE functional with SOC, we also found the defect levels is located between the CBM and VBM (shown in Figure SI4b in the SI), and a deep-level trap state is formed. The electron in the deep-level trap favors the iodine vacancy migration from the top-surface layer to the subsurface layer. Compared with that in the MAI–terminated surface, the iodine vacancy in the PbI_2–terminated surface was more susceptible to form deep-level traps due to the presence of dangling bonds on the top-layer Pb ions. The reason is that two deep-level trapped electrons are needed to induce such migration for the MAI-terminated surface while one is enough for the PbI_2– terminated surface. This could be a reason that previous experimental studies showed that the MAI–excess $MAPbI_3$ films have higher PL intensity (i.e., lower nonradiative recombination) than

the stoichiometric or PbI$_2$–excess MAPbI$_3$ films.[33, 79]

We further studied the V_I^+ vacancy with two excess electrons (ie. V_I^-). Figures 3e and 3f show the optimized structures with two additional electrons introduced to the structures with the top-surface layer vacancy and the subsurface layer vacancy respectively. As shown in the figures, there is not spontaneous iodine migration upon optimization. The charge density difference (Figures SI6c and SI6d in the SI) shows that the added electron in the structures in both Figures 3e and 3f is localized at two Pb ions. Moreover, a Pb–Pb covalent bond was formed between the two Pb originally bonded to the removed iodine in both cases. The Pb-Pb bond length for the two structures is 3.26 and 3.39 Å respectively. The MLWF analysis shows that the two Pb ions for the two structures were reduced to a Pb$_2^{2+}$ dimer in both cases (Figures SI3e ~ SI3h in the SI). Similar to V_I^0, we found that V_I^- at the subsurface layer (Figure 3f) is more stable by –4.5 kcal/mol than that at the top-surface layer (Figure 3e). As shown in Figure 3h, the total DOS of V_I^- at the subsurface layer (Figure 3f) has an intragap state, which is closely related to favorability of the vacancy at the subsurface layer. Using the HSE functional with SOC, we also found the defect levels located between the CBM and VBM (shown in Figure SI4c in the SI), and a deep-level trap state is formed. We performed CI–NEB to study the migration process (Figure 3i), and the activation energy was found to be +19.7 kcal/mol. Due to the strong Pb-Pb covalent bond, the activation energy of iodide migration is large.
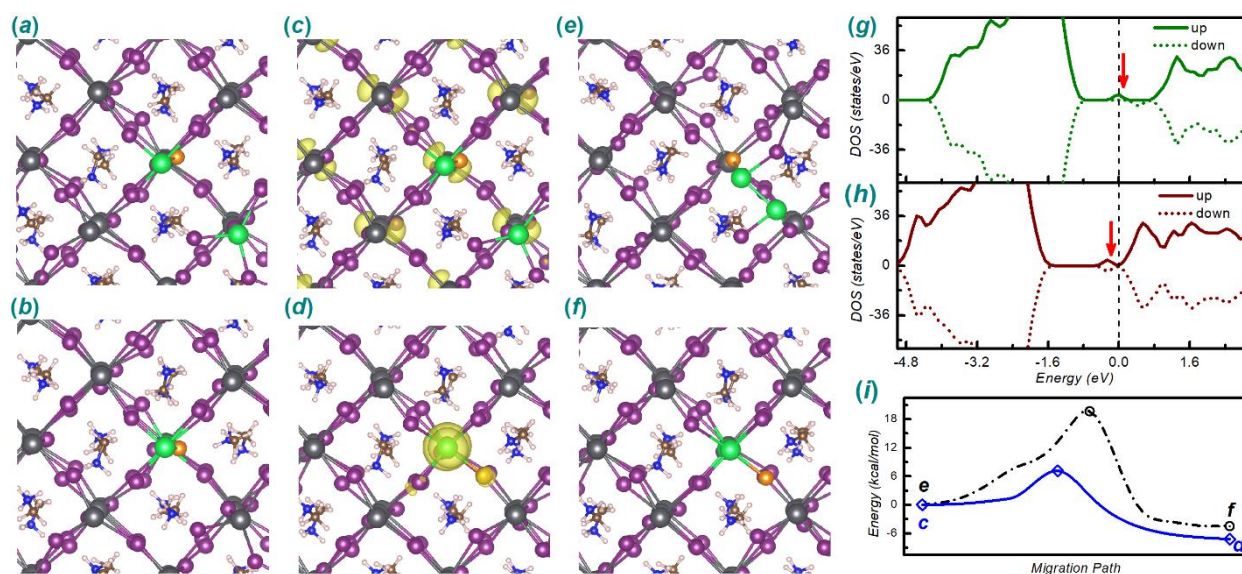
Figure 3. (a) & (b) The relaxed structure with a V_I^+ vacancy initially at the **P1** and the **P2** position, respectively, in the PbI$_2$−terminated surface. (c) & (d) The relaxed structure with a V_I^0 vacancy initially at the **P1** and the **P2** position, respectively, in the PbI$_2$−terminated surface. (e) & (f) The relaxed structure with a V_I^- vacancy initially at the **P1** and the **P2** position, respectively, in the PbI$_2$−terminated surface. (g) & (h) The total density of states for the structure in Figure 3d and Figure 3f, respectively, with the Fermi level set at 0 eV. The red arrow indicates the intragap state. (i) The energy profile for iodine migration from the structure in Figure 3c to the structure in Figure 3d, and from the structure in Figure 3e to the structure in Figure 3f. The side views of the structures in this figure are shown in Figure SI7 in the SI. The Pb ions originally bonded to the removed iodide are marked as green spheres. The spin densities are shown as the yellow contour surfaces. The color codes for the other atoms are the same as those in Figure 1.

3.3 Electron detrapping at the MAI–terminated surface

The trapped electrons can be eliminated via different processes such as recombination with photoinduced holes and removal by the humid air or the electron transport layers (e.g., fullerene derivatives and metal oxides). Here, we focus on humid air elimination of the trapped electrons. Since hydroxyl radicals (OH) can readily form at the MAPbI$_3$/metal oxide (e.g., ZnO) interface under illumination and the humid air condition,[80, 81] we also study here the role of the OH species in eliminating excess electrons. For the charge detrapping process, an OH radical can only abstract one electron. However, molecular O$_2$ can abstract one electron (or two electrons), converting to superoxide (or peroxide) during the chemisorption process. We chose the surface Pb ion as the adsorption site for the OH radical and oxygen species. We also studied H$_2$O molecule adsorption on the perovskite surface for comparison. As will be discussed below, the H$_2$O molecule only physisorbs on the perovskite surface and the excess electrons do not transfer to the H$_2$O molecule. Therefore, the relaxed structures of H$_2$O adsorption are only shown in the SI. For the MAI– terminated MAPbI$_3$ surfaces, the energetically favorable structures in Figures 2a (V_I^+), 2c (V_I^0) and 2f (V_I^-) were selected as the templates for the adsorption study.

First, we respectively placed H$_2$O, O$_2$ and OH on the perovskite surface with a V_I^+ vacancy (**M1**

position) as shown in Figure 2a for the case without excess electrons. The adsorption energies are listed in Table 1. The H_2O molecule was found to physisorb on the surface (Figure SI8a in the SI), and the adsorption energy is –37.0 kcal/mol. The MLWF analysis confirmed that the H_2O remains a neutral molecule upon adsorption. The O_2 adsorption structure is shown in Figure 4a. The O_2 physisorbs on Pb ions with a small adsorption energy of –16.1 kcal/mol. The spin density distribution (Figure 4a) and the MLWF analysis (Figures SI9a and SI9b in the SI) confirms that there is no electron abstraction by the O_2. On the other hand, for OH, as shown in the spin density distribution in Figure 4b, we found that an electron was abstracted from the perovskite surface by the OH radical. The spin density in the figure shows that the resulting hole is delocalized over the inorganic framework of PbI_3^-. The MLWF analysis in Figures SI9c and SI9d in the SI also confirms that the OH radical is converted to an OH^- ion. A Pb–O covalent bond is also formed.

Moreover, two H···O hydrogen bonds between the OH radical and two nearby MA cations in the surface. Since it is chemisorption, the adsorption energy of OH is more negative (–64.9 kcal/mol) compared to those with H_2O and O_2. For all three cases above, the iodine vacancy remains at the top-surface layer. We also calculated the OH radical adsorption energies on the pristine surfaces, which equals –63.1 kcal/mol. Without the excess electron, the OH radical adsorption energies on the defective surface is close to that of the pristine surface.

Then, we respectively placed H_2O, O_2 and OH on the perovskite surface in Figure 2c with a V_I^0 vacancy (**M1** position) for the case with one excess electron. In this case, the excess electron is in the shallow-level trap. The adsorption energies are shown in Table 1. As shown in Figure 4c, with one excess electron, O_2 chemisorbs on the perovskite surface. The MLWF analysis indicates that the O_2 is converted to a superoxide (Figures SI10a and SI10b in the SI). The adsorption energy is –49.5 kcal/mol, which is more negative than O_2 adsorption without the excess electron (–16.1 kcal/mol). For the case with an OH radical, the excess electron was also abstracted by the OH radical upon adsorption (Figure 4d). The MLWF analysis in Figures SI10c and SI10d in the SI confirms that the OH radical is converted to an OH^- ion. The adsorption energy is –106.7 kcal/mol, which is also more negative than the case in Figure 4b without the excess electron (–64.9 kcal/mol) and the OH radical adsorption energies on the pristine surfaces (-63.1 kcal/mol). This shows that

the presence of the defect levels leads to the more negative OH adsorption energies. Therefore, the excess electron enhances the adsorption of the O_2 and OH species to the surface which is often the first step of the degradation reaction. This means that the presence of the shallow-level traps can accelerate the photodegradation of MAPbI$_3$ under the humid air condition. On the other hand, as shown in Table 1, the H_2O adsorption energy changed little in the presence of an excess electron. The adsorption structure is shown in Figures SI8b and SI8c in the SI. The MLWF analysis shown in the figures suggests that the charge state of the H_2O remains zero. Again, for all these three cases, the iodine vacancy remains at the top-surface layer upon adsorption.

We then studied the cases with two excess electrons. H_2O, O_2 and OH were respectively placed on the perovskite surface with a V_I^- vacancy and the two excess electrons are in the deep-level trapped states (Figure 2f). The adsorption energies are shown in Table 1. In this case, before adsorption, the iodine vacancy is situated more favorably at the subsurface layer (**M2** position). Similar to the previous cases, H_2O only physisorbs on the surface. The adsorption energy is –33.7 kcal/mol. The MLWF analysis (Figures SI8d and SI8e in the SI) shows that the charge state of the H_2O remains zero. On the other hand, Figure 4e shows the O_2 adsorption structure. The spin-polarized calculation was performed in this case but we found no net spin for this structure. The two excess electrons are abstracted by the O_2 molecule as it chemisorbs on the surface forming a peroxide. Simultaneously, a proton from the nearby MA cations spontaneously transfers to the resulting peroxide in this proton coupled–electron transfer (PCET) process, forming an OOH^- ion. The formation of an OOH^- ion was also confirmed by the MLWF analysis shown in Figures SI11a and SI11b in the SI. On top of that, the iodine vacancy at the subsurface **M2** position spontaneously migrates back to the top-surface **M1** position due to the loss of two electrons. The adsorption energy of the O_2 molecule is –90.8 kcal/mol which is more negative than the cases without excess electrons and with one excess electron. Therefore, the two excess electrons in the deep-level traps enhance the photodegradation of MAPbI$_3$ under the humid air condition. The two transferred electrons come from the original Pb^{2+} dimer and the Pb_2^{2+} dimer is oxidized back to two Pb^{2+} ions. This suggests that in the presence of O_2, the excess electrons prefer to transfer to the O_2 over reducing the Pb^{2+} ions to Pb^+ or Pb^0. This is consistent with the previous experimental

studies which found that Pb nanoparticles (or metallic Pb) as a degradation product can only form in the vacuum condition rather than in the air.[73, 82] On the other hand, the optimized structure shown in Figure 4e has slight distortion from the original lattice positions. We manually moved these ions back to their original lattice positions and the optimized structure is shown in Figure 4f. We found that this structure in is more stable by -1.8 kcal/mol. The CI–NEB calculation showed that the activation energy for the ion migration process is $+6.2$ kcal/mol (Figure 4j).

Next, we studied the OH adsorption on the MAI-terminated surface with a V_I^- vacancy (Figure 4g). The OH radical was found to abstract one of the two excess electrons from the surface. The spin density distribution in Figure 4g shows that the remaining excess electron is mainly trapped in the two Pb ions originally bonded to the removed iodine (i.e. the green lead ions). The V_I^0 vacancy was found to remain at the subsurface layer although, as stated above for the case with one excess electron in the perovskite surface, it is more favorable for the V_I^0 vacancy to situate at the top-surface layer. We performed the CI–NEB calculation to study the iodine migration process for the V_I^0 vacancy to return to the top-surface layer (Figure 4j). The activation energy was found to be only $+1.5$ kcal/mol. The final state (Figure 4h) is slightly more stable than the initial state by -1.5 kcal/mol. The spin density distribution in Figure 4h shows that the remaining excess electron is delocalized over all the Pb ions. After that, we added another OH radical on the surface. The optimized structure (Figure 4i) shows that the additional OH radical abstracts the remaining excess electron from the surface. The MLWF analysis also confirmed that the two excess electrons were abstracted by the two OH species, forming two OH^- ions (Figures SI11c and SI11d in the SI). After detrapping the two excess electrons, the iodine vacancy at the top-surface layer (**M1** position) remains more favorable. Overall, our results suggest that the presence of the electrons in deep-level traps favors vacancies at subsurface layer. The trapping and detrapping process induces iodine migration between the top-surface layer and the subsurface layer.
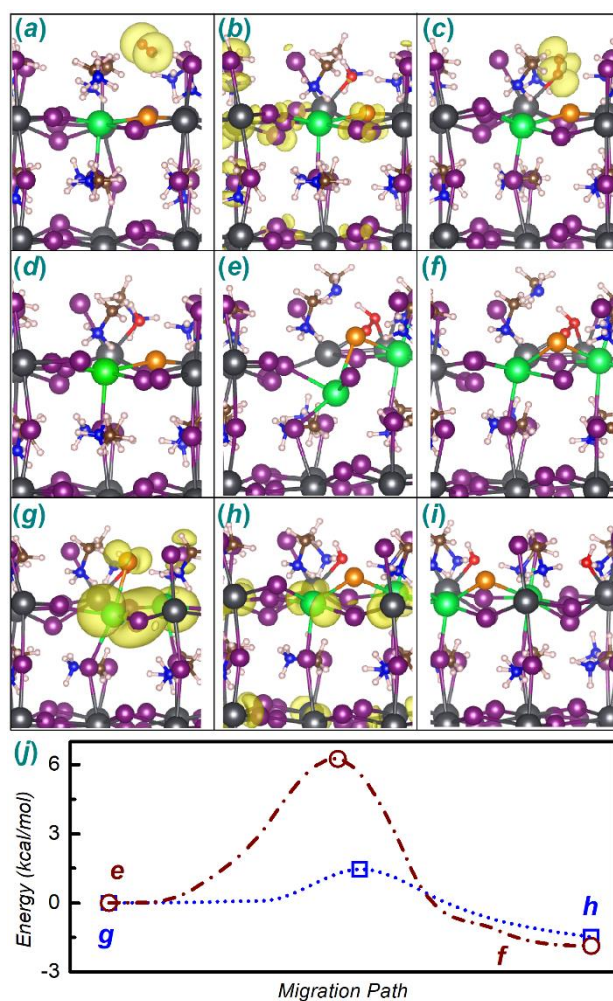
Figure 4. (a) & (b) The adsorption of an O_2 and OH on the structure in Figure 2a, respectively. (c) & (d) The adsorption of an O_2 and OH on the structure in Figure 2c, respectively. (e) & (g) The adsorption of an O_2 and OH on the structure in Figure 2f, respectively. (f) & (h) The final state of the structure in Figure 4e and Figure 4g after ion migration, respectively. (i) The adsorption with the second OH on the structure in Figure 4h. (j) The energy profile for the above two migration processes. The Pb ions originally bonded to the removed iodide are marked as green spheres. The spin densities are shown as the yellow contour surfaces. The color codes for the other atoms are the same as those in Figure 1.

Table 1 The adsorption energies in kcal/mol of the H_2O, O_2 and OH on the MAI–terminated surfaces with different types of vacancies. We marked "Y" (or "N") when there is (or is not) vacancy migration induced by the adsorption and electron abstraction processes.

	H_2O	O_2	1st OH	2nd OH

	E_{ads}	Migration	E_{ads}	Migration	E_{ads}	Migration	E_{ads}	Migration
V_I^+	–37.0	N	–16.1	N	–64.9	N	–	–
V_I^0	–34.4	N	–49.5	N	–106.7	N	–	–
V_I^-	–33.7	N	–90.8	Y	–106.8	Y	–102.0	N

3.4 Electron detrapping at the PbI$_2$–terminated surface

For the PbI$_2$–terminated MAPbI$_3$ surface, we used the energetically favorable structures in Figures 3a (V_I^+), 3d (V_I^0) and 3f (V_I^-) as the templates for the adsorption study. First, we respectively placed the H$_2$O, O$_2$ and OH species on the perovskite surface in Figure 3a which has no excess electrons. The iodine vacancy is originally at the top-surface layer (**P1** position). Table 2 shows the adsorption energies for the different adsorbates. Again, the H$_2$O molecule was found to weakly interact with the perovskite surface (Figure SI12a in the SI) with a small adsorption energy of –17.5 kcal/mol. Similarly, O$_2$ also physisorbs on the surface (Figure 5a) with a small adsorption energy of –16.9 kcal/mol. The MLWF analysis (Figures SI13a and SI13b in the SI) confirmed that the charge state of O$_2$ is zero. On the other hand, as shown in Figure 5b, the OH radical chemisorbs on the surface bonding with a surface Pb ion ($d_{(Pb-O)}$ = 2.15 Å) with a large adsorption energy of –41.0 kcal/mol. The net spin density (Figure 5b) localizes around the OH and the top layer of the inorganic PbI$_3^-$ framework. The MLWF analysis suggests that the OH radical becomes an OH$^-$ ion (Figures SI13c and SI13d in the SI). The iodine vacancy remains at the top-surface layer due to the absence of the deep-level trapped electrons. We also calculated the OH radical adsorption energies on the pristine surfaces, which equals –42.6 kcal/mol. Without the excess electron, the OH radical adsorption energies on the defective surface is close to that of the pristine surface.

Then, we respectively placed H$_2$O, O$_2$ and OH on the PbI$_2$-terminated perovskite surface with an iodine vacancy and one excess electron (V_I^0). The iodine vacancy is originally more favorable at the subsurface layer (**P2** position). Table 2 shows the adsorption energies for the different adsorbates. The H$_2$O was found to only weakly interact with the perovskite surface (Figures SI12b and SI12c in the SI). On the other hand, the O$_2$ spontaneously abstracts the excess electron upon adsorption (Figure 5c). The MLWF analysis in Figures SI14a and SI14b in the SI indicates that

the O_2 is converted to a superoxide. The original Pb_2^{3+} dimer at the subsurface is oxidized to become two Pb^{2+} ions. Due to the detrapping of the deep-level electron, the iodine vacancy spontaneously migrates to the top-surface layer. Moreover, the resulting superoxide occupies the iodine vacancy (**P2** position) at the top-surface layer, and two oxygens form two Pb-O covalent bonds with two surface Pb. As shown in Table 2, the adsorption energy is –44.0 kcal/mol, which is significantly more negative than the case without the excess electron (–16.9 kcal/mol). There is no obvious distortion of the structure in Figure 5c from the original lattice structure. For OH adsorption, as shown in Figure 5d, a Pb-O bond is formed between a surface Pb ion and the OH. The adsorption energy for OH radical is –76.5 kcal/mol, which is also more negative than the case in Figure 4b without the excess electron (–41.0 kcal/mol) and the OH radical adsorption energies on the pristine surfaces (-42.6 kcal/mol). Therefore, the more negative OH adsorption energies is due to the presence of the defect levels. The MLWF analysis in Figures SI14c and SI14d in the SI indicates that the OH is converted to an OH^- ion. The subsurface iodine vacancy spontaneously migrates to the top-surface layer. However, the optimized structure has a slight distortion, and some ions (especially for the green Pb ion on the top-surface layer) are away from the original lattice positions. The CI–NEB calculation (Figure 5j) were applied to study the ion diffusion back to their original lattice positions. The final structure is shown in Figure 5e. The activation energy is +5.2 kcal/mol, and the finial state is more stable that the initial state by -4.1 kcal/mol.

We next placed H_2O, O_2 and OH respectively on the perovskite surface with an iodine vacancy and two excess electrons (i.e. the structure in Figure 3f). The iodine vacancy is originally at the subsurface layer (**P2** position). For the case with H_2O, the two excess electrons do not transfer to the H_2O. The H_2O only physisorbs on the surface with an adsorption energy of –17.0 kcal/mol (Figure SI12d and SI12e in the SI). On the other hand, the O_2 chemisorbs on the surface (Figure 5f). The MLWF analysis (Figures SI15a and SI15b in the SI) shows that the O_2 molecule spontaneously abstracts the two excess electrons, forming a peroxide species. As shown in Table 2, the adsorption energy of the O_2 is increased to -62.6 kcal/mol, which is significantly more negative than the case with an excess electron (-44.0 kcal/mol). Without the two deeply-trapped electrons, the iodine vacancy spontaneously migrates to the top-surface layer. At the same time,

the resulting peroxide occupied the iodine vacancy. The original Pb_2^{2+} dimer is oxidized to form two Pb^{2+} ions. The two oxygen atoms of the resulting peroxide were also found to form three Pb-O bonds with two surface Pb ions. There is no obvious distortion for the atoms in this case from their original lattice positions. For OH adsorption, as shown in Figure 5g, one OH radical abstracts only one of the two excess electrons. The spin density distribution in Figure 5g shows that the remaining excess electron is still mainly shared by the two Pb ions originally bonding to the removed iodine. As shown in Table 2, the adsorption energy of the OH is –72.1 kcal/mol. However, due to the loss of one excess electron, the Pb-Pb bond increases from 3.26 to 3.55 Å. Since the V_I^0 at the subsurface layer is more stable than that at the top-surface layer in the case with one excess electron in the surface, there is no iodine migration. We further added another OH radical to the surface. The adsorption energy was found to be -78.3 kcal/mol and the remaining excess electron spontaneously transfers to the OH. The MLWF analysis (Figures SI15c and SI15d in the SI) also confirms that the two excess electrons are abstracted by the two OH radicals, forming two OH^- ions. Due to the removal of two deeply-trapped electrons, the iodine vacancy spontaneously migrates from the subsurface layer to the top-surface layer. However, the optimized structure (Figure 5h) has a slight distortion. Some atoms (especially for the green Pb ion on the top-surface layer) are away from their lattice sites. The CI–NEB calculation (Figure 5j) was applied to study the ion diffusion process. The activation energy was calculated to be +6.7 kcal/mol, and the finial state is more stable that the finial state by -5.8 kcal/mol.
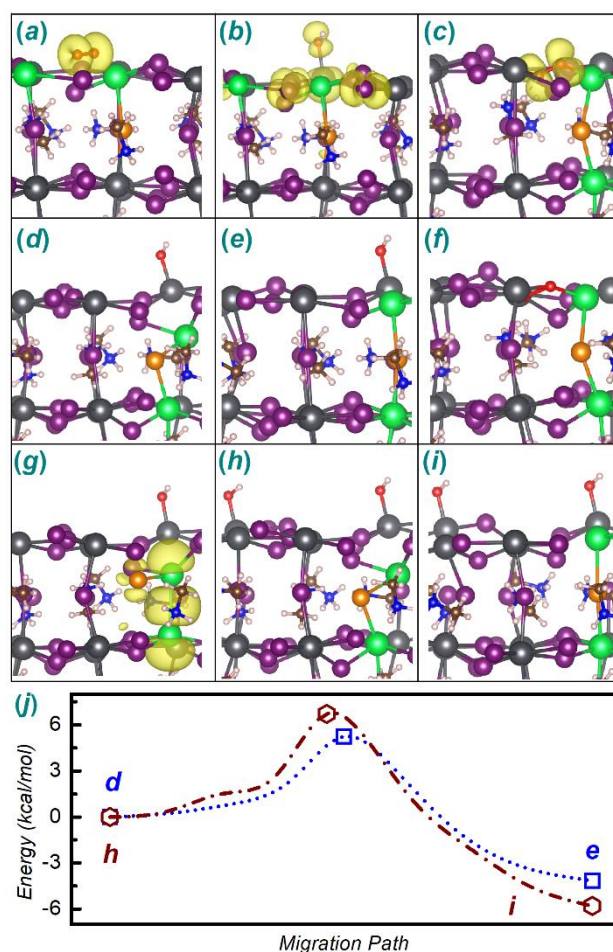
Figure 5 (a) & (b) The adsorption of an O_2 and OH on the structure in Figure 3a, respectively. (c) & (d) The adsorption of an O_2 and OH on the structure in Figure 3d, respectively. (f) & (g) The adsorption of an O_2 and OH on the structure in Figure 3f, respectively. (h) The adsorption with the second OH on the structure in Figure 5g. (e) & (i) The final state of the structure in Figure 5d and Figure 5h during ion migration, respectively. (j) The energy profiles for the above two migration processes. The Pb ions originally bonded to the removed iodide are marked as green spheres. The spin densities are shown as the yellow contour surfaces. The color codes for the other atoms are the same as those in Figure 1.

Table 2 The adsorption energies of the H_2O, O_2 and OH on the PbI_2–terminated surfaces with different types of vacancies. We marked "Y" (or "N") if there is (or is not) vacancy migration induced by the adsorption and electron abstraction processes.

	H_2O		O_2		1st OH		2nd OH	
	E_{ads}	Migration	E_{ads}	Migration	E_{ads}	Migration	E_{ads}	Migration

V_I^+	−17.5	N	−16.9	N	−41.0	N	–	–
V_I^0	−17.6	N	−44.0	Y	−76.5	Y	–	–
V_I^-	−17.0	N	−62.6	Y	−72.1	N	−78.3	Y

3.5 Electron trapping and detrapping in bulk MAPbI₃

In this subsection, we studied the electron trapping and detrapping processes in bulk MAPbI$_3$. The behavior of two iodine vacancies in bulk perovskite are also studied. We considered two different types of vacancy arrangement: one is that the two iodine vacancies in bulk MAPbI$_3$ are next-nearest neighbors (nonadjacent), while the other is that the two iodine vacancies are adjacent. Herein, we mainly considered vacancy migration between the two arrangements. For the structures with two next-nearest iodine vacancies and two adjacent iodine vacancies, we denoted here the **B1** and **B2** structures, respectively. Firstly, for the electron trapping process, and we respectively introduced one excess electron to the **B1** and **B2** structures (Figures 6a and 6b). The spin density plot for the **B1** structure (Figure 6a) shows that the excess electron delocalizes around the Pb ions. However, for the **B2** structure (Figure 6b), the excess electron mainly localizes at two of the Pb ions, forming a Pb$_2^{3+}$ ion. Therefore, for the **B2** structure, one V_I^0 vacancy and one V_I^+ vacancy was formed. Moreover, we found that the structure with two adjacent iodine vacancies (Figure 6b) is more stable by −2.3 kcal/mol than the structure with two nonadjacent iodine vacancies (Figure 6a). We performed the CI–NEB calculation to study the iodine migration process from the **B1** to **B2** structures, and the activation energy was found to be +9.0 kcal/mol. Although here we studied iodine vacancy migration from the next-nearest-neighbor to the adjacent configuration. The vacancies can in fact migrate over a long distance. There are two steps for such long-range migration: (1) The iodine vacancies separated by a long distance migrate to the next-nearest sites (**B1** structure). The mechanism of this stage is similar to the iodine vacancy migration proposed by previous studies.[38, 75, 76, 78] (2) iodine vacancies migrate from the **B1** structure to the **B2** structure. The schematic diagram of long-range iodine migration in bulk MAPbI$_3$ are shown in Figure SI16 in the SI.

We then added the second excess electron to both the **B1** and the **B2** structures. The optimized

structures are shown in Figures 6c and 6d. A covalent Pb-Pb bond is formed (i.e., Pb_2^{2+} ion) in both cases, and the corresponding Pb-Pb distance is 3.62 and 3.57 Å, respectively. Therefore, for both structures, one V_I^- vacancy and one V_I^+ vacancy was formed, respectively. We found that the structure with two adjacent iodine vacancies (Figure 6d) is more stable by –2.1 kcal/mol than the structure with two nonadjacent iodine vacancies (Figure 6c). We performed the CI–NEB calculation to study the iodine migration process (from Figure 6c to 6d), and the activation energy is +8.4 kcal/mol.

Furthermore, we studied the electron detrapping process in bulk $MAPbI_3$. After abstracting an excess electron from the structure in Figure 6b or two excess electrons from the structure in Figure 6d, two adjacent V_I^+ vacancies were formed in the bulk $MAPbI_3$. The optimized structure is shown in Figure 6e. However, the structure is unstable by +8.7 kcal/mol than the structure with two nonadjacent (next-nearest) V_I^+ vacancies (Figure 6f). We performed the CI–NEB calculation to study the iodine migration process (from Figure 6e to 6f), and the activation energy is +8.6 kcal/mol.

To evaluate the thermostability of the trapped states, we also calculated the thermodynamic ionization levels for the structure with two adjacent iodine vacancies (i.e. the structures in Figures 6b, 6d, 6e) by using the HSE functional with SOC. The charge states for the structures in the Figure 6b, 6d, 6e are +1, 0, and +2, respectively. As shown in Figure 6h, the three transition levels are below the edge of the CBM. Therefore, the deep trapped V_I^- vacancy (with two excess electrons in the supercell) is thermodynamically stable. The iodine vacancies formed deep trap states via the iodine migration process.

The DFT results showed that without the excess electrons, the iodine vacancies are unlikely to cluster together. The excess electrons facilitate the clustering of the iodine vacancies together. Using DFT calculations, we also studied the following structures: (1) three nonadjacent iodine vacancies in the bulk $MAPbI_3$; (2) three adjacent iodine vacancies in the bulk $MAPbI_3$. The results are shown in Figure SI17 in the SI. We found that with electron trapping, the structure with three

adjacent iodine vacancies in the bulk MAPbI$_3$ is more stable. However, after electron detrapping, the structure with three nonadjacent iodine vacancies in bulk MAPbI$_3$ is more stable. This further supports the finding that the excess electrons facilitate the iodine vacancies to cluster together. This could explain the formation of metallic Pb as one of the MAPbI$_3$ photo-degradation products in vacuum.
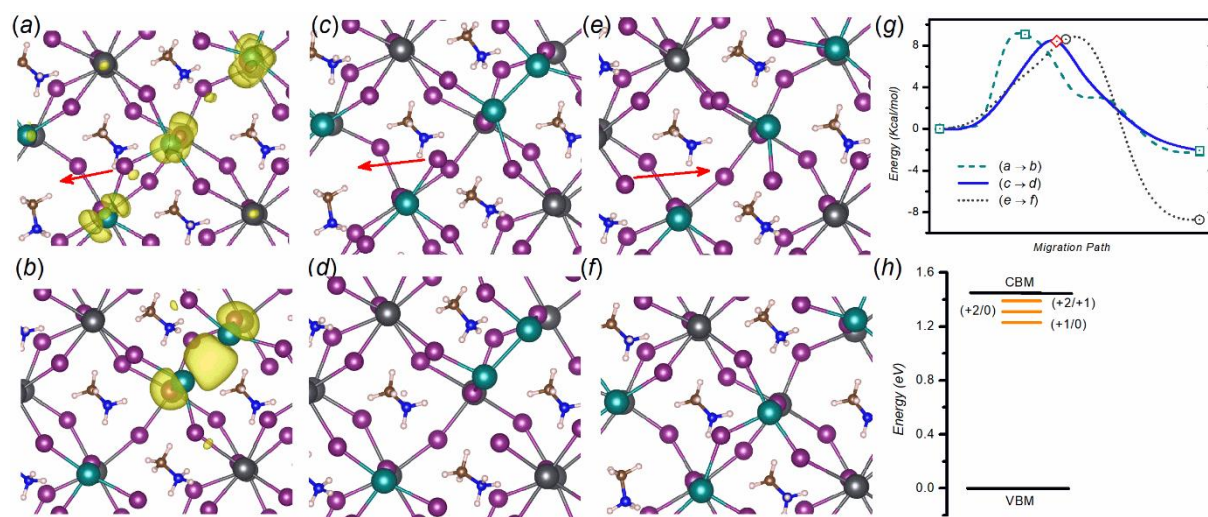

Figure 6 (a) & (b) The relaxed **B1** and **B2** structure with one excess electron, respectively. (c) & (d) The relaxed **B1** and **B2** structure with two excess electrons, respectively. (e) & (f) The relaxed **B2** and **B1** structure without excess electron, respectively. (g) The energy profiles for the three migration processes. The red arrows in (a), (c) and (e) denote the directions of the iodine diffusion. (h) The thermodynamic ionization levels for the **B2** structure. The Pb ions bonded to the removed iodide are marked as dark cyan spheres. The spin densities are shown as the yellow contour surfaces. The color codes for the other atoms are the same as those in Figure 1.

3.6 The possible origin of photoinduced ion migration and hysteresis behavior

In this subsection, we discuss the possible origin of photoinduced ion migration and the $J–V$ hysteresis behavior. Snaith and coworkers suggested that a combination of mobile ions and traps are responsible for $J–V$ hysteresis.[26] In this work, we found that, without excess electrons, it is more favorable for the iodine vacancy V_I^+ to locate at the top-surface layer for both the MAI–terminated (i.e., MAI–excess) and PbI$_2$–terminated (i.e., PbI$_2$–excess) MAPbI$_3$ surfaces. Under the forward bias condition when a large number of trapped electrons accumulate at the defects,[31,]

[32] the top-surface iodine vacancies become unstable and migrate to the subsurface layer. While two deep-level trapped electrons are needed to induce such migration for the MAI-terminated surface, one is enough for the PbI_2–terminated surface. This suggests the higher propensity for the PbI_2–terminated to have deep-level electron trap states and exhibit the J–V hysteresis behavior. This is consistent with the experimental studies which found that the MAI–excess $MAPbI_3$ films have higher photoluminescence intensity (i.e., lower nonradiative recombination) than that of the stoichiometric or PbI_2–excess $MAPbI_3$ films.[33, 79]

When the trapped electrons are released under the short-circuit condition,[31, 32] the iodine vacancies migrate from the subsurface layer back to the top-surface layer. Therefore, the excess electrons trapping and detrapping in the deep–level states induces iodine migration and the J–V hysteresis behavior. Since excess electrons can also be generated under illumination, such a behavior should be dependent on the photon dose. In fact, previous experimental works also observed photon–dependent iodine migration and hysteresis effects.[20, 83] Furthermore, it has been found that hysteresis effects were generally higher in the photovoltaic devices using PbI_2-excess $MAPbI_3$ samples than those using stoichiometric or MAI–excess $MAPbI_3$ samples.[22, 28, 33] One possible reason is that the PbI_2–terminated (PbI_2–excess) surface is more susceptible to form deep–level trapped states. Our work also explains why previous experimental works[84, 85] found that suppressing charge accumulations in the interface of the perovskite/electron transport layers contributes to the reduction of the hysteresis effect.

4 Conclusion

Using DFT techniques, we studied the properties of iodine vacancies on the MAI–terminated and PbI_2–terminated surfaces. The V_I^+ vacancy was found to be more favorable to stay at the top-surface layer. It is because removing an I^- ion at the top-surface layer of the MAI–terminated surface only breaks one Pb–I bond, rather than two Pb-I bonds if the vacancy is created at the subsurface layer. For the PbI_2–terminated surface, there are two MA cations interacting with a top-surface layer I^- ion, while there are four MA cations interacting with the subsurface layer I^- ion. Therefore, it is energetically favorable to create a V_I^+ vacancy at the top-surface.

We then studied the effects of excess electrons on the vacancy stability. We first introduced one excess electron to the MAI–terminated surface with one V_I^+ vacancy. The excess electron was found to be in a shallow-level trap state. The resulting V_I^0 vacancy remains at the top-surface layer. However, by introduction one excess electron to form the V_I^0 vacancy in the PbI$_2$–terminated surface, a deep–level trapped state is formed. The vacancy preferentially migrates to the subsurface layer leading to the formation of a Pb$_2^{3+}$ dimer. Therefore, the excess electron in the deep-level trap facilitates the iodine vacancy migration from top-surface layer to subsurface layer as well as the Pb$_2^{3+}$ dimer formation. Previous theoretical studies using TDDFT also found that the deep traps can be formed in defective MAPbI$_3$ perovskite (e.g. iodine vacancies).[47] These strongly localized electrons at the iodine vacancies facilitate the formation of Pb-Pb covalent bonds. By introducing two excess electrons, the V_I^- vacancy preferentially locates at the subsurface layer for both the MAI-terminated and PbI$_2$–terminated surfaces with the formation of the deep-level traps and a Pb$_2^{2+}$ dimer. Therefore, for the MAI–terminated surface, the iodine vacancy migrates from the top-surface layer to the subsurface layer. The resulting Pb$_2^{2+}$ or Pb$_2^{3+}$ dimer could be the precursor of lead nanoparticles (one of MAPbI$_3$ degradation products in vacuum).[72, 73] Based on the above results, the PbI$_2$–terminated (i.e., PbI$_2$–excess) surface exhibits a higher tendency to capture excess electrons to form deep-level trapped states, leading to the migration of top-surface iodine vacancy to the subsurface. This could be a possible reason that the MAI–excess MAPbI$_3$ have higher photoluminescence intensity (i.e., lower nonradiative recombination) than that of the stoichiometric or PbI$_2$–excess MAPbI$_3$ films.[33, 79]

To study the electron detrapping process, we placed the H$_2$O, OH radical and O$_2$ on the surfaces. They are expected to respectively abstract zero, one and two excess electrons. For the surfaces without excess electrons or with only a shallow-level trapped electron, the vacancy remains at the top surface upon adsorption. However, for the surfaces with deep-level trapped electrons, we found that the iodine vacancy migrated from the subsurface layer back to the top-surface layer during the chemisorption of the OH radicals and O$_2$ due to electron detrapping. The adsorption

strength of the OH radicals and O_2 were also enhanced by the presence of excess electron no matter whether the electrons are in the shallow or deep trapped states. The Pb_2^{2+} or Pb_2^{3+} dimer was oxidized back to two Pb^{2+} ions during the detrapping process. The excess electrons preferentially transfer to the OH and O_2 over the Pb ions. This could be the reason why lead nanoparticles (or metallic leads) as a degradation product can only be formed in the vacuum condition.[73, 82]

Furthermore, we studied the electron trapping and detrapping processes in bulk $MAPbI_3$. We found that with electron trapping, the structure with two adjacent iodine vacancies in the bulk $MAPbI_3$ is more stable. The excess electrons facilitate the clustering of the two iodine vacancies together and form deep trap states via iodine migration process. However, after electron detrapping, the structure with two adjacent iodine vacancies in bulk $MAPbI_3$ become unstable, which facilitates the formation of two nonadjacent iodine vacancies via iodine migration process. The iodine vacancies are unlikely to cluster together in the absence of excess electrons. Finally, we discussed the possible mechanisms for photoinduced ion migration and the hysteresis behavior. Through this study, we found that excess electrons trapped in both the shallow-level and deep-level states enhance photodegradation of $MAPbI_3$ under the humid air condition. However, the electrons in the deep-level traps play a significantly more important role in facilitating photoinduced ion migration and the hysteresis behavior.

Acknowledgements

References

1. W. S. Yang, B.-W. Park, E. H. Jung, N. J. Jeon, Y. C. Kim, D. U. Lee, S. S. Shin, J. Seo, E. K. Kim, J. H. Noh and S. I. Seok, *Science*, 2017, **356**, 1376-1379.

2. A. Kojima, K. Teshima, Y. Shirai and T. Miyasaka, *J. Am. Chem. Soc.*, 2009, **131**, 6050-6051.

3. N.-G. Park, M. Grätzel, T. Miyasaka, K. Zhu and K. Emery, *Nat. Energy*, 2016, **1**, 16152.

4. M. D. Sampson, J. S. Park, R. D. Schaller, M. K. Y. Chan and A. B. F. Martinson, *J. Mater. Chem. A*, 2017, **5**, 3578-3588.

5. P.-P. Sun, Q.-S. Li, S. Feng and Z.-S. Li, *Phys. Chem. Chem. Phys.*, 2016, **18**, 14408-14418.

6. M. Roknuzzaman, K. Ostrikov, H. Wang, A. Du and T. Tesfamichael, *Sci. Rep.*, 2017, **7**, 14025.

7. T. Zhao, D. Wang and Z. Shuai, *Synth. Met.*, 2017, **225**, 108-114.

8. S. D. Stranks, G. E. Eperon, G. Grancini, C. Menelaou, M. J. P. Alcocer, T. Leijtens, L. M. Herz, A. Petrozza and H. J. Snaith, *Science*, 2013, **342**, 341-344.

9. T. C. Jellicoe, J. M. Richter, H. F. J. Glass, M. Tabachnyk, R. Brady, S. E. Dutton, A. Rao, R. H. Friend, D. Credgington, N. C. Greenham and M. L. Böhm, *J. Am. Chem. Soc.*, 2016, **138**, 2941-2944.

10. I. L. Braly and H. W. Hillhouse, *J. Phys. Chem. C*, 2016, **120**, 893-902.

11. T. Zhao, W. Shi, J. Xi, D. Wang and Z. Shuai, *Sci. Rep.*, 2016, **6**, 19968.

12. B. Murali, E. Yengel, C. Yang, W. Peng, E. Alarousu, O. M. Bakr and O. F. Mohammed, *ACS Energy Lett.*, 2017, **2**, 846-856.

13. A. R. Srimath Kandada, S. Neutzner, V. D'Innocenzo, F. Tassone, M. Gandini, Q. A. Akkerman, M. Prato, L. Manna, A. Petrozza and G. Lanzani, *J. Am. Chem. Soc.*, 2016, **138**, 13604-13611.

14. N. De Marco, H. Zhou, Q. Chen, P. Sun, Z. Liu, L. Meng, E.-P. Yao, Y. Liu, A. Schiffer and Y. Yang, *Nano Lett.*, 2016, **16**, 1009-1016.

15. W. Zhang, Y. Ding, Y. Jiang, M. Zheng, S. Wu, X. Lu, M. Zeng, X. Gao, Q. Wang, G. Zhou, J.-M. Liu, K. Kempa and J. Gao, *RSC Adv.*, 2017, **7**, 39523-39529.

16. W. Nie, H. Tsai, J.-C. Blancon, F. Liu, C. C. Stoumpos, B. Traore, M. Kepenekian, O.

Durand, C. Katan, S. Tretiak, J. Crochet, P. M. Ajayan, M. Kanatzidis, J. Even and A. D. Mohite, *Adv. Mater.*, 2017, **30**, 1703879.

17. V. Adinolfi, W. Peng, G. Walters, O. M. Bakr and E. H. Sargent, *Adv. Mater.*, 2018, **30**, 1700764.

18. E. Mosconi, D. Meggiolaro, H. J. Snaith, S. D. Stranks and F. De Angelis, *Energy Environ. Sci.*, 2016, **9**, 3180-3187.

19. E. T. Hoke, D. J. Slotcavage, E. R. Dohner, A. R. Bowring, H. I. Karunadasa and M. D. McGehee, *Chem. Sci.*, 2015, **6**, 613-617.

20. D. W. deQuilettes, W. Zhang, V. M. Burlakov, D. J. Graham, T. Leijtens, A. Osherov, V. Bulović, H. J. Snaith, D. S. Ginger and S. D. Stranks, *Nat. Commun.*, 2016, **7**, 11683.

21. N. Aristidou, C. Eames, I. Sanchez-Molina, X. Bu, J. Kosco, M. S. Islam and S. A. Haque, *Nat. Commun.*, 2017, **8**, 15218.

22. T. P. Gujar, T. Unger, A. Schonleber, M. Fried, F. Panzer, S. van Smaalen, A. Kohler and M. Thelakkat, *Phys. Chem. Chem. Phys.*, 2018, **20**, 605-614.

23. M. Lorenzon, L. Sortino, Q. Akkerman, S. Accornero, J. Pedrini, M. Prato, V. Pinchetti, F. Meinardi, L. Manna and S. Brovelli, *Nano Lett.*, 2017, **17**, 3844-3853.

24. S. G. Motti, M. Gandini, A. J. Barker, J. M. Ball, A. R. Srimath Kandada and A. Petrozza, *ACS Energy Lett.*, 2016, **1**, 726-730.

25. Y. Tian, M. Peter, E. Unger, M. Abdellah, K. Zheng, T. Pullerits, A. Yartsev, V. Sundstrom and I. G. Scheblykin, *Phys. Chem. Chem. Phys.*, 2015, **17**, 24978-24987.

26. S. van Reenen, M. Kemerink and H. J. Snaith, *J. Phys. Chem. Lett.*, 2015, **6**, 3808-3814.

27. B. Wu, K. Fu, N. Yantara, G. Xing, S. Sun, T. C. Sum and N. Mathews, *Adv. Energy Mater.*, 2015, **5**, 1500829.

28. H. Yu, H. Lu, F. Xie, S. Zhou and N. Zhao, *Adv. Funct. Mater.*, 2016, **26**, 1411-1419.

29. J.-W. Lee, S.-G. Kim, S.-H. Bae, D.-K. Lee, O. Lin, Y. Yang and N.-G. Park, *Nano Lett.*, 2017, **17**, 4270-4276.

30. F. Cai, L. Yang, Y. Yan, J. Zhang, F. Qin, D. Liu, Y.-B. Cheng, Y. Zhou and T. Wang, *J. Mater. Chem. A*, 2017, **5**, 9402-9411.

31. W. Tress, N. Marinova, T. Moehl, S. M. Zakeeruddin, M. K. Nazeeruddin and M. Gratzel,

Energy Environ. Sci., 2015, **8**, 995-1004.

32. B. Chen, M. Yang, S. Priya and K. Zhu, *J. Phys. Chem. Lett.*, 2016, **7**, 905-917.

33. T. J. Jacobsson, J.-P. Correa-Baena, E. Halvani Anaraki, B. Philippe, S. D. Stranks, M. E. F. Bouduban, W. Tress, K. Schenk, J. Teuscher, J.-E. Moser, H. Rensmo and A. Hagfeldt, *J. Am. Chem. Soc.*, 2016, **138**, 10331-10343.

34. Z. Xiao and Y. Yan, *Adv. Energy Mater.*, 2017, **7**, 1701136.

35. M. L. Agiorgousis, Y.-Y. Sun, H. Zeng and S. Zhang, *J. Am. Chem. Soc.*, 2014, **136**, 14570-14575.

36. W. Shan and W. A. Saidi, *J. Phys. Chem. Lett.*, 2017, **8**, 5935-5942.

37. R. Dong, Y. Fang, J. Chae, J. Dai, Z. Xiao, Q. Dong, Y. Yuan, A. Centrone, X. C. Zeng and J. Huang, *Adv. Mater.*, 2015, **27**, 1912-1918.

38. J.-H. Yang, W.-J. Yin, J.-S. Park and S.-H. Wei, *J. Mater. Chem. A*, 2016, **4**, 13105-13112.

39. W. W. Wang, J. S. Dang, R. Jono, H. Segawa and M. Sugimoto, *Chem. Sci.*, 2018, **9**, 3341-3353.

40. M.-H. Du, *J. Phys. Chem. Lett.*, 2015, **6**, 1461-1466.

41. L.-y. Wei, W. Ma, C. Lian and S. Meng, *J. Phys. Chem. C*, 2017, **121**, 5905-5913.

42. W. Ming, S. Chen and M.-H. Du, *J. Mater. Chem. A*, 2016, **4**, 16975-16981.

43. D. A. Egger, L. Kronik and A. M. Rappe, *Angew. Chem. In. Ed.*, 2015, **54**, 12437-12441.

44. Y. Liu, K. Palotas, X. Yuan, T. Hou, H. Lin, Y. Li and S.-T. Lee, *ACS Nano*, 2017, **11**, 2060-2065.

45. H. Uratani and K. Yamashita, *J. Phys. Chem. Lett.*, 2017, **8**, 742-746.

46. D. Meggiolaro, S. G. Motti, E. Mosconi, A. J. Barker, J. Ball, C. Andrea Riccardo Perini, F. Deschler, A. Petrozza and F. De Angelis, *Energy Environ. Sci.*, 2018, **11**, 702-713.

47. G. Nan, X. Zhang, M. Abdi-Jalebi, Z. Andaji-Garmaroudi, S. D. Stranks, G. Lu and D. Beljonne, *Adv. Energy Mater.*, 2018, **8**, 1702754.

48. H. Yuan, E. Debroye, G. Caliandro, K. P. F. Janssen, J. van Loon, C. E. A. Kirschhock, J. A. Martens, J. Hofkens and M. B. J. Roeffaers, *ACS Omega*, 2016, **1**, 148-159.

49. S. T. Birkhold, E. Zimmermann, T. Kollek, D. Wurmbrand, S. Polarz and L. Schmidt-Mende, *Adv. Funct. Mater.*, 2017, **27**, 1604995.

50.   Y. Ren, I. W. H. Oswald, X. Wang, G. T. McCandless and J. Y. Chan, *Cryst. Growth Des.*, 2016, **16**, 2945-2951.

51.   E. Mosconi, E. Ronca and F. De Angelis, *J. Phys. Chem. Lett.*, 2014, **5**, 2619-2625.

52.   M. Saliba, S. Orlandi, T. Matsui, S. Aghazada, M. Cavazzini, J.-P. Correa-Baena, P. Gao, R. Scopelliti, E. Mosconi, K.-H. Dahmen, F. De Angelis, A. Abate, A. Hagfeldt, G. Pozzi, M. Graetzel and M. K. Nazeeruddin, *Nat. Energy*, 2016, **1**, 15017.

53.   L. Zhang and P. H. L. Sit, *J. Mater. Chem. A*, 2017, **5**, 9042-9049.

54.   L. Zhang and P. H. L. Sit, *J. Mater. Chem. A*, 2017, **5**, 23976-23986.

55.   P. Hohenberg and W. Kohn, *Phys. Rev.*, 1964, **136**, B864–B871.

56.   W. Kohn and L. J. Sham, *Phys. Rev.*, 1965, **140**, A1133–A1138.

57.   P. Giannozzi, S. Baroni, N. Bonini, M. Calandra, R. Car, C. Cavazzoni, D. Ceresoli, G. L. Chiarotti, M. Cococcioni, and I. Dabo, *et al.*, *J. Phys.: Condens. Matter*, 2009, **21**, 395502.

58.   J. P. Perdew, K. Burke and M. Ernzerhof, *Phys. Rev. Lett.*, 1996, **77**, 3865–3868.

59.   D. Vanderbilt, *Phys. Rev. B*, 1990, **41**, 7892–7895.

60.   S. Grimme, *J. Comput. Chem.*, 2006, **27**, 1787-1799.

61.   V. Barone, M. Casarin, D. Forrer, M. Pavone, M. Sambi and A. Vittadini, *J. Comput. Chem.*, 2009, **30**, 934-939.

62.   G. Henkelman and H. Jónsson, *J. Chem. Phys.*, 2000, **113**, 9978-9985.

63.   N. Marzari and D. Vanderbilt, *Phys. Rev. B* 1997, **56**, 12847.

64.   I. Souza, N. Marzari and D. Vanderbilt, *Phys. Rev. B*, 2001, **65**, 035109.

65.   P. H. L. Sit, F. Zipoli, J. Chen, R. Car, M. H. Cohen and A. Selloni, *Chem. Eur. J.*, 2011, **17**, 12136-12143.

66.   J. Chen and P. H. L. Sit, *Catal. Today*, 2018, **314**, 179-186.

67.   A. A. Mostofi, J. R. Yates, Y.-S. Lee, I. Souza, D. Vanderbilt and N. Marzari, *Comput. Phys. Commun.*, 2008, **178**, 685-699.

68.   J. Heyd, G. E. Scuseria and M. Ernzerhof, *J. Chem. Phys.*, 2003, **118**, 8207-8215.

69.   J. Gebhardt and A. M. Rappe, *J. Mater. Chem. A*, 2018, **6**, 14560-14565.

70.   D. Meggiolaro, E. Mosconi and F. De Angelis, *ACS Energy Lett.*, 2017, **2**, 2794-2798.

71.   T. Baikie, Y. Fang, J. M. Kadro, M. Schreyer, F. Wei, S. G. Mhaisalkar, M. Graetzel and

T. J. White, *J. Mater. Chem. A*, 2013, **1**, 5628-5641.

72. J. Schoonman, *Chem. Phys. Lett.*, 2015, **619**, 193-195.

73. X. Tang, M. Brandl, B. May, I. Levchuk, Y. Hou, M. Richter, H. Chen, S. Chen, S. Kahmann, A. Osvet, F. Maier, H.-P. Steinruck, R. Hock, G. J. Matt and C. J. Brabec, *J. Mater. Chem. A*, 2016, **4**, 15896-15903.

74. S. Meloni, T. Moehl, W. Tress, M. Franckevičius, M. Saliba, Y. H. Lee, P. Gao, M. K. Nazeeruddin, S. M. Zakeeruddin, U. Rothlisberger and M. Graetzel, *Nat. Commun.*, 2016, **7**, 10334.

75. C. Eames, J. M. Frost, P. R. F. Barnes, B. C. O'Regan, A. Walsh and M. S. Islam, *Nat. Commun.*, 2015, **6**, 7497.

76. J. M. Azpiroz, E. Mosconi, J. Bisquert and F. De Angelis, *Energy Environ. Sci.*, 2015, **8**, 2118-2127.

77. C.-J. Tong, W. Geng, O. V. Prezhdo and L.-M. Liu, *ACS Energy Lett.*, 2017, **2**, 1997-2004.

78. J. Haruyama, K. Sodeyama, L. Han and Y. Tateyama, *J. Am. Chem. Soc.*, 2015, **137**, 10048-10051.

79. S. Ham, Y. J. Choi, J.-W. Lee, N.-G. Park and D. Kim, *J. Phys. Chem. C*, 2017, **121**, 3143-3148.

80. J. Yang, B. D. Siempelkamp, E. Mosconi, F. De Angelis and T. L. Kelly, *Chem. Mater.*, 2015, **27**, 4229-4236.

81. L. Zhang and P. H. L. Sit, *J. Phys. Chem. C*, 2015, **119**, 22370-22378.

82. Q. Sun, P. Fassl, D. Becker-Koch, A. Bausch, B. Rivkin, S. Bai, P. E. Hopkinson, H. J. Snaith and Y. Vaynzof, *Adv. Energy Mater.* , 2017, **7**, 1700977.

83. M. Pazoki, T. J. Jacobsson, S. H. T. Cruz, M. B. Johansson, R. Imani, J. Kullgren, A. Hagfeldt, E. M. J. Johansson, T. Edvinsson and G. Boschloo, *J. Phys. Chem. C*, 2017, **121**, 26180-26187.

84. W. Bo, F. Kunwu, Y. Natalia, X. Guichuan, S. Shuangyong, S. T. Chien and M. Nripan, *Adv. Energy Mater.*, 2015, **5**, 1500829.

85. J. H. Heo, M. S. You, M. H. Chang, W. Yin, T. K. Ahn, S.-J. Lee, S.-J. Sung, D. H. Kim and S. H. Im, *Nano Energy*, 2015, **15**, 530-539.

TOC Figure